

## Algorithmic scatter correction in dual-energy digital mammography

Xi Chen, Robert M. Nishikawa, Suk-tak Chan, Beverly A. Lau, Lei Zhang, and Xuanqin Mou

Citation: *Medical Physics* **40**, 111919 (2013); doi: 10.1118/1.4826173

View online: <http://dx.doi.org/10.1118/1.4826173>

View Table of Contents: <http://scitation.aip.org/content/aapm/journal/medphys/40/11?ver=pdfcov>

Published by the American Association of Physicists in Medicine

---

## Advertisement:

**DoseWise in the OR**  
10 easy steps for effective dose management

These steps help you adhere closely to the ALARA principle (As Low As Reasonably Achievable) for X-ray dose management.

- 1. Proper system setup**  
Correctly position and align the X-ray system to ensure optimal image quality and dose management.
- 2. Use protective shielding**  
Use lead shields to protect patients and staff from unnecessary radiation exposure.
- 3. Remove X-ray grid**  
Remove the X-ray grid when not needed to reduce scatter radiation and improve image quality.
- 4. Position image detector**  
Position the image detector correctly to ensure optimal image quality and dose management.
- 5. Maintain distance**  
Maintain a safe distance from the X-ray source to reduce radiation exposure to staff.

Teach your staff to be DoseWise.  
Order your free poster now!

[www.philips.com/dosewiseintheor](http://www.philips.com/dosewiseintheor) **PHILIPS**

# Algorithmic scatter correction in dual-energy digital mammography

Xi Chen

*Institute of Image Processing and Pattern Recognition, Xi'an Jiaotong University, Xi'an, Shaanxi 710049, China*

Robert M. Nishikawa<sup>a)</sup>

*Department of Radiology, The University of Chicago, Chicago, Illinois 60637*

Suk-tak Chan

*Department of Health Technology and Informatics, The Hong Kong Polytechnic University, Hung Hom, Hong Kong*

Beverly A. Lau<sup>b)</sup>

*Department of Radiology, The University of Chicago, Chicago, Illinois 60637*

Lei Zhang

*Department of Computing, The Hong Kong Polytechnic University, Hung Hom, Hong Kong*

Xuanqin Mou<sup>c)</sup>

*Institute of Image Processing and Pattern Recognition, Xi'an Jiaotong University, Xi'an, Shaanxi 710049, China*

(Received 29 March 2013; revised 6 September 2013; accepted for publication 6 October 2013; published 25 October 2013)

**Purpose:** Small calcifications are often the earliest and the main indicator of breast cancer. Dual-energy digital mammography (DEDM) has been considered as a promising technique to improve the detectability of calcifications since it can be used to suppress the contrast between adipose and glandular tissues of the breast. X-ray scatter leads to erroneous calculations of the DEDM image. Although the pinhole-array interpolation method can estimate scattered radiations, it requires extra exposures to measure the scatter and apply the correction. The purpose of this work is to design an algorithmic method for scatter correction in DEDM without extra exposures.

**Methods:** In this paper, a scatter correction method for DEDM was developed based on the knowledge that scattered radiation has small spatial variation and that the majority of pixels in a mammogram are noncalcification pixels. The scatter fraction was estimated in the DEDM calculation and the measured scatter fraction was used to remove scatter from the image. The scatter correction method was implemented on a commercial full-field digital mammography system with breast tissue equivalent phantom and calcification phantom. The authors also implemented the pinhole-array interpolation scatter correction method on the system. Phantom results for both methods are presented and discussed. The authors compared the background DE calcification signals and the contrast-to-noise ratio (CNR) of calcifications in the three DE calcification images: image without scatter correction, image with scatter correction using pinhole-array interpolation method, and image with scatter correction using the authors' algorithmic method.

**Results:** The authors' results show that the resultant background DE calcification signal can be reduced. The root-mean-square of background DE calcification signal of 1962  $\mu\text{m}$  with scatter-uncorrected data was reduced to 194  $\mu\text{m}$  after scatter correction using the authors' algorithmic method. The range of background DE calcification signals using scatter-uncorrected data was reduced by 58% with scatter-corrected data by algorithmic method. With the scatter-correction algorithm and denoising, the minimum visible calcification size can be reduced from 380 to 280  $\mu\text{m}$ .

**Conclusions:** When applying the proposed algorithmic scatter correction to images, the resultant background DE calcification signals can be reduced and the CNR of calcifications can be improved. This method has similar or even better performance than pinhole-array interpolation method in scatter correction for DEDM; moreover, this method is convenient and requires no extra exposure to the patient. Although the proposed scatter correction method is effective, it is validated by a 5-cm-thick phantom with calcifications and homogeneous background. The method should be tested on structured backgrounds to more accurately gauge effectiveness. © 2013 American Association of Physicists in Medicine. [<http://dx.doi.org/10.1118/1.4826173>]

Key words: dual energy, mammography, scatter correction, calcification

## 1. INTRODUCTION

Breast cancer is a major health concern for women. Calcifications are one of the earliest and main indicators of breast cancer and mammography is the gold standard for breast cancer screening. Thus, the visualization and detection of calcifications in mammography play a crucial role in reducing the mortality rate of breast cancer. Calcifications are usually smaller than 1.0 mm and mainly composed of calcium compounds such as apatite, calcium oxalate, and calcium carbonate.<sup>1</sup> Calcifications have greater x-ray attenuation coefficients than the surrounding breast tissues, so they are more visible on homogeneous soft-tissue backgrounds. However, the visualization of calcifications could be obscured in mammograms because of overlapping of tissue structures.<sup>2,3</sup> Tissue structures in mammograms arise from the differences of the x-ray attenuation coefficients between adipose tissue, glandular tissue, ducts, vessels, and soft-tissue masses. Calcifications, especially smaller ones, can be difficult to detect.

Dual-energy digital mammography (DEDM) is considered as a promising technique to improve the detection precision of calcifications. The principles of dual-energy (DE) imaging have been discussed extensively in literature.<sup>2,4-8</sup> Alvarez and Macovski<sup>4</sup> demonstrated that within the diagnostic energy range, the linear attenuation coefficient can be represented as a linear combination of attenuation coefficients of two basis materials. As a result, x-ray measurements can be taken at two different energies and combined nonlinearly to produce two basic images. These two basic images can be linearly combined to produce images with the advantages of increased conspicuity or visualization due to the removal of overlapping breast structures, and the ability for selective material cancellation. In DEDM, high-energy (HE) and low-energy (LE) images of the breast are acquired using two different x-ray spectra. The HE and LE images can be combined to suppress the contrast between adipose and glandular tissues of the breast and subsequently generate the DE calcification image. Under ideal imaging conditions, when the image data are free of scatter and other noises, DEDM could be used to determine the size of calcifications and the breast glandular ratio.<sup>9</sup>

Early research on the feasibility of DE mammography included optimal HE and LE spectra selection,<sup>7</sup> selection of inverse-map functions,<sup>10</sup> influence of detectors,<sup>11-13</sup> and experimental studies.<sup>2,13</sup> In 2002, Lemacks *et al.*<sup>9</sup> presented a theoretical framework to calculate the quantum noise in DE calcification image. Their results were presented in terms of contrast-to-noise ratio (CNR) under various imaging conditions, including the x-ray spectra, calcification size, tissue composition, and breast thickness. Based on the work of Lemacks *et al.*,<sup>9</sup> Kappadath *et al.* made a series of investigations on DEDM, including calibration and inverse-map functions,<sup>14</sup> quantitative evaluation,<sup>3</sup> scatter and nonuniformity correction,<sup>15</sup> postimage processing, and noise reduction technique.<sup>16,17</sup> DEDM has also been investigated and evaluated by other investigators.<sup>18-22</sup>

One important concern for DEDM imaging is the scattered radiations arising from the interaction of x-ray photons and

materials in the patient. In the experiment of Cooper III *et al.*,<sup>23</sup> the measured scatter-to-primary ratios (SPRs) at 28 kVp for a 4-cm-thick breast phantom were 0.3960 for 0% glandular, 0.3560 for 43% glandular, and 0.4260 for 100% glandular. In clinical full-field digital mammography system, antiscatter grids are usually used during image acquisition for their efficiency in the suppression of scatter; however, they do not completely eliminate the scatter. In Kappadath and Shaw's experiment, they measured scatter fractions for a wedge phantom with an antiscatter grid using a full-field digital mammography system (Senographe 2000D, GE Medical Systems, Milwaukee, WI). They found that scatter fractions ranged from 17% to 22% and from 20% to 25% for the LE and HE images, respectively. Scattered radiation contributes mainly to noise increase and contrast degradation in a single acquisition,<sup>24</sup> in DE imaging it will result in further degeneration, like the serious deterioration of the signal of interest.

Since scatter contamination in the LE and HE images can lead to erroneous calculation of the DE signals, the scatter fraction should be estimated and used to calculate the amount of scatter in the DE image for subtraction. Kappadath and Shaw<sup>15</sup> adopted a pinhole-array interpolation method for scatter correction in DEDM. This method employed a lead sheet containing an array of pinholes to acquire spot measurements of the primary radiation, and then the scattered radiation at the spot locations can be obtained. The scatter signal in the entire full-field image was estimated by fitting a smooth surface to the scatter at the spot locations. This technique needs extra exposures for the spot measurements, complicates the manipulation, and is impractical for DEDM in clinic. Other methods to reduce scattered radiations, such as applying an air gap,<sup>25</sup> employing a slot scanning system,<sup>26,27</sup> or multislit scanning system,<sup>28</sup> require a completely new system design for mammography unit.

We proposed a scatter correction algorithm which was verified by Monte Carlo simulation<sup>29</sup> and a simple breast phantom experiment.<sup>30</sup> This algorithm calculates the scatter components by the LE and HE images themselves exploiting the characteristic that scatter in mammograms is a quantity of low-frequency and the fact that most pixels in mammograms are noncalcification pixels. It is convenient and there is no extra dose to patients. In this paper, we present the performance of this algorithmic scatter correction method by breast and calcification phantom studies implemented on a commercial full-field digital mammography system. We also implemented the pinhole-array interpolation scatter correction method on the system. Phantom results for both methods are presented and discussed. The total entrance-skin exposure and mean glandular dose used for the LE and HE images were constrained to be similar to screening examination levels.

## 2. THEORY

### 2.A. Dual-energy digital mammography calculation

Lemacks *et al.*<sup>9</sup> proposed a numerical framework to perform the DEDM calculation. They assumed that there are three attenuating materials in the breast: adipose tissue

(thickness  $t_a$ ), glandular tissue (thickness  $t_g$ ), and calcification (thickness  $t_c$ ). Depending on the distribution of materials, the transmitted fluence incident on the detector is given by

$$F(E) = F_0(E) \exp[-\mu_a(E)t_a - \mu_g(E)t_g - \mu_c(E)t_c], \quad (1)$$

where  $F_0(E)$  and  $F(E)$  are the incident photon fluence on the surface of the breast and the transmitted fluence, respectively; and  $\mu_a(E)$ ,  $\mu_g(E)$ , and  $\mu_c(E)$  are the linear attenuation coefficients of adipose tissue, glandular tissue, and calcification, respectively. Ideally, it would be best to estimate the thicknesses  $t_a$ ,  $t_g$ , and  $t_c$  of the three attenuating materials. However, only two unknowns can be solved in DEDM. In a mammographic examination, breast is usually compressed to a uniform thickness  $T$  ( $T = t_a + t_g + t_c$ ) that is automatically measured by the x-ray system. On the other hand, the contribution of

calcifications to the total breast thickness can be ignored because the calcifications are small in size and sparsely present in breast, i.e.,  $T \approx t_a + t_g$ . With the total breast thickness  $T$  known, the three unknowns  $t_a$ ,  $t_g$ , and  $t_c$  can be expressed as two unknowns: glandular ratio  $g = t_g/T \approx t_g/(t_a + t_g)$  and calcification thickness  $t_c$ . Now, Eq. (1) can be rewritten as<sup>9,14</sup>

$$F(E) = F_0(E) \exp[-\mu_a(E)T - g(\mu_g(E) - \mu_a(E))T - \mu_c(E)t_c]. \quad (2)$$

In DE imaging calculations, a reference signal  $I_r$  is needed to change the dynamic range of the intensity values. The exposure data  $D$  are defined as the ratio of the reference signal  $I_r$  to the transmitted signal  $P$ . The LE and HE signals  $D_l(t_c, g)$  and  $D_h(t_c, g)$  are measured independently using x-ray beams at different kVps:

$$D_j(t_c, g) = \frac{I_{rj}}{P_j} = \frac{I_{rj}}{\left( \int F_{0j}(E) \exp[-\mu_a(E)T - g(\mu_g(E) - \mu_a(E))T - \mu_c(E)t_c] Q(E) dE \right)}, \quad j = l, h, \quad (3)$$

where  $Q(E)$  is the detector response.

In medical diagnostic x-ray imaging modalities, poly-energetic spectra are often used, which results in a nonlinear relationship between  $(D_l, D_h)$  and  $(t_c, g)$ .<sup>4-6,10,14</sup> In this paper, an inverse-map function:

$$t_c = \frac{a_0 + a_1 D_l + a_2 D_h + a_3 D_l^2 + a_4 D_l D_h + a_5 D_h^2 + a_6 D_l^3 + a_7 D_l^2 D_h + a_8 D_l D_h^2 + a_9 D_h^3}{1 + b_0 D_l + b_1 D_h + b_2 D_l^2 + b_3 D_l D_h + b_4 D_h^2} \quad (4)$$

was used to describe the relationship between calcification thickness  $t_c$  and LE and HE image signal  $(D_l, D_h)$ .<sup>10</sup> The coefficients  $a_m$  and  $b_n$  ( $m = 0, \dots, 9$ ;  $n = 0, \dots, 4$ ) are determined by a calibration procedure.<sup>5</sup> By measuring the transmission intensities of various combinations of glandular ratio and aluminum thickness (to simulate calcifications) with LE and HE spectra, the groups of calibration data  $(D_l, D_h, g, t_c)$  can be acquired to estimate the coefficients  $a_m$  and  $b_n$ .

## 2.B. Scatter representation

In Eqs. (3) and (4), the scattered radiation has not been considered. In practice, if we want to get the accurate DE calculation results, scatter effects should be taken into account. Actually, the signal measured in each pixel of the detector is the sum of signal from primary radiation,  $P$ , and that from scattered radiation,  $S$ . For any pixel in the LE or HE image, let

$$I'_j = P_j + S_j, \quad j = l, h, \quad (5)$$

where  $P_j$  is the primary radiation,  $S_j$  is the scattered radiation, and  $I'_j$  is the measured signal. Then,  $D_j$  ( $j = l, h$ ) can be rewritten as

$$D_j = \frac{I_{rj}}{(I'_j - S_j)}, \quad j = l, h. \quad (6)$$

Substituting Eq. (6) into Eq. (4), we would like to solve for the scatter components  $S_l$  and  $S_h$ . It can be seen that the coefficients  $a_m$  and  $b_n$  ( $m = 0, \dots, 9$ ;  $n = 0, \dots, 4$ ), reference signals  $I_{rl}$  and  $I_{rh}$ , and measured signals  $I'_l$  and  $I'_h$  are all known values, and there are three unknowns  $t_c$ ,  $S_l$ , and  $S_h$  to be solved. Obviously, it is impossible to solve three unknowns using just one equation. However, scatter in mammograms is a quantity of low-frequency in the spatial domain because the breast is usually compressed to a largely uniform thickness during mammography. Therefore, the scattered radiation of one pixel can be approximated as those of the neighbor pixels, which will greatly decrease the quantities of unknown variables. As illustrated in Fig. 1, we selected some pixels in the image,  $A_i$  ( $i = 1, \dots, 8$ ),  $B_i$  ( $i = 1, \dots, 6$ ), and  $C_i$  ( $i = 1, \dots, 3$ ). Pixels  $B_i$  and  $C_i$  lie between pixels  $A_i$ . Therefore, using linear interpolation, scattered radiation of pixel  $B_i$  or  $C_i$  can be represented

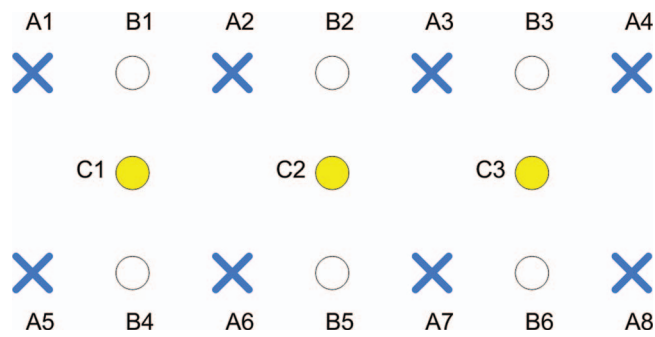


FIG. 1. Schematic drawing of the selected pixels,  $A_i$  ( $i = 1, \dots, 8$ ),  $B_i$  ( $i = 1, \dots, 6$ ), and  $C_i$  ( $i = 1, \dots, 3$ ). Pixels  $B_i$  and  $C_i$  lie between pixels  $A_i$ . Scattered radiation of pixel  $B_i$  or  $C_i$  can be represented as the average of scattered radiation of pixel  $A_i$ .

as the average of scattered radiation of pixel  $A_i$ . For examples, scattered radiation of pixel B1 can be represented as

$$S_{B1j} = \frac{(S_{A1j} + S_{A2j})}{2}, \quad j = l, h, \quad (7)$$

and scattered radiation of pixel C1 can be represented as

$$S_{C1j} = \frac{(S_{A1j} + S_{A2j} + S_{A5j} + S_{A6j})}{4}, \quad j = l, h. \quad (8)$$

## 2.C. Scatter estimation

For an imaged object, both LE and HE images are acquired without moving the object. We can sample  $N$  pixels in the LE image and the corresponding pixels in the HE image. These  $N$  pixel pairs can be put into two categories: independent pixel pairs and dependent pixel pairs.  $k_1$  pairs belong to independent pixel pairs whose scatter are unknowns, such as pixels  $A_i$  ( $i = 1, \dots, 8$ ) in Fig. 1;  $k_2$  ( $k_2 > k_1$ ) pairs are dependent pixel pairs whose scatter are represented by those of independent pairs, such as pixels  $B_i$  ( $i = 1, \dots, 6$ ), C1, C2, and C3.

Since most pixels in mammograms are noncalcification pixels, the sampled pixels can be considered as noncalcification pixels, i.e., their corresponding  $t_c$  is zero. For all the sampled pixels, the variance and the mean of  $t_c$  are nearly to zero. Then, we can set up an equation set with  $N$  equations, of the form shown in Eq. (4). In this equation set, there are  $2k_1$  unknowns  $S_{ij}$  ( $i = 1, \dots, k_1$ ;  $j = l, h$ ) to be determined. Provided  $N = k_1 + k_2 > 2k_1$ , the  $2k_1$  unknowns  $S_{ij}$  can be determined by forcing the least-squares estimate of the variance of  $t_c$  of the  $N$  pixel pairs to be zero. So the scattered radiation of the  $k_1$  pixel pairs  $S_{ij}$  can be determined, scattered radiation of other pixels can be obtained by interpolation. Then, a pixel by pixel estimate of the scatter fields for the LE and HE images can be generated.

## 3. MATERIALS AND METHODS

### 3.A. Dual-energy imaging techniques

The mammography system used in this study was a full-field digital mammography system (Senographe Essential, GE Medical Systems, Milwaukee, WI). The detector

consisted of a CsI:Tl converter layer coupled with an aSi:H + TFT flat-panel detector. The image size was  $3062 \times 2394$  with a pixel size of  $100 \mu\text{m}$ . For-processing “raw” images were used for our DE calculations. Previous investigations<sup>7,9</sup> have shown that the DE calcification image noise decreases with greater separation between the LE and HE spectra. In this work, LE and HE spectra were chosen to maximize the spectral separation allowed by the hardware options on the mammography system used. The imaging conditions selected in this study were similar to those in the previous studies,<sup>9,15,17</sup> the total mean-glandular dose and entrance-skin exposure were constrained to typical screening examination levels: 28 kVp at 50 mAs for LE imaging and 48 kVp at 12.5 mAs for HE imaging.

The system has two focal spots and two targets: 100 and  $300 \mu\text{m}$ , Mo target and Rh target. Only the  $300 \mu\text{m}$  focal spot on the Rh target could be used at 48 kVp in this experiment. (The generator limit is 49 kVp.) The Rh target was used for both the LE and HE, to avoid misregistration due to the shift in focal spot offset.<sup>15</sup> K-edge for Mo is at 20 keV and the peaks for Rh are at 20.3 and 22.7 keV. For a Rh/Mo target/filter combination, the Rh peaks will be filtered and the final DE calcification image will be distorted. Finally, the mammography machine does not allow the user to select the Rh/Mo combination. Therefore, we used the  $300 \mu\text{m}$  focal spot on the Rh target with Rh filter for LE and HE imaging in this experiment. The source to image distance was 66 cm and the antiscatter grid and the compression plate were used during image acquisition.

### 3.B. Phantom for imaging

For this study, a breast phantom and a calcification phantom were used as the imaged object. The breast phantom (Model 017, Computerized Imaging Reference Systems Inc., Norfolk, VA) was a rectangular block with dimension of  $12 \times 10 \times 4 \text{ cm}^3$  [Fig. 2(a)]. This model was a density step phantom that simulated different ratios of glandular and adipose tissues. The glandular ratio ranged from 0% to 100% in six steps, 0%, 30%, 45%, 50%, 70%, and 100%. There was a water equivalent bolus on each end. The average elemental composition of the human breast being modeled was based on the individual elemental composition of adipose and glandular tissues reported by Hammerstein *et al.*<sup>31</sup> The inner clear acrylic section of the breast phantom was not included in our DE calculation and comparison, since acrylic is not a stable representation of breast tissue across a wide x-ray energy range. The calcification phantom [Fig. 2(b)] was a rectangular block of 50% glandular ratio with 42 embedded calcification clusters. Each calcification cluster consisted of nine  $\text{Al}_2\text{O}_3$  crystals (Computerized Imaging Reference Systems Inc., Norfolk, VA) used to simulate calcifications in a  $3 \times 3$  pattern. The  $\text{Al}_2\text{O}_3$  crystals were organized by size into six rows with nominal size ranges (provided by CIRS) of 180–230, 230–280, 280–330, 330–380, 380–430, and 430–480  $\mu\text{m}$ . The calcification size varied along the shorter side but not along the longer (chest wall) side. The dimension of the calcification phantom was

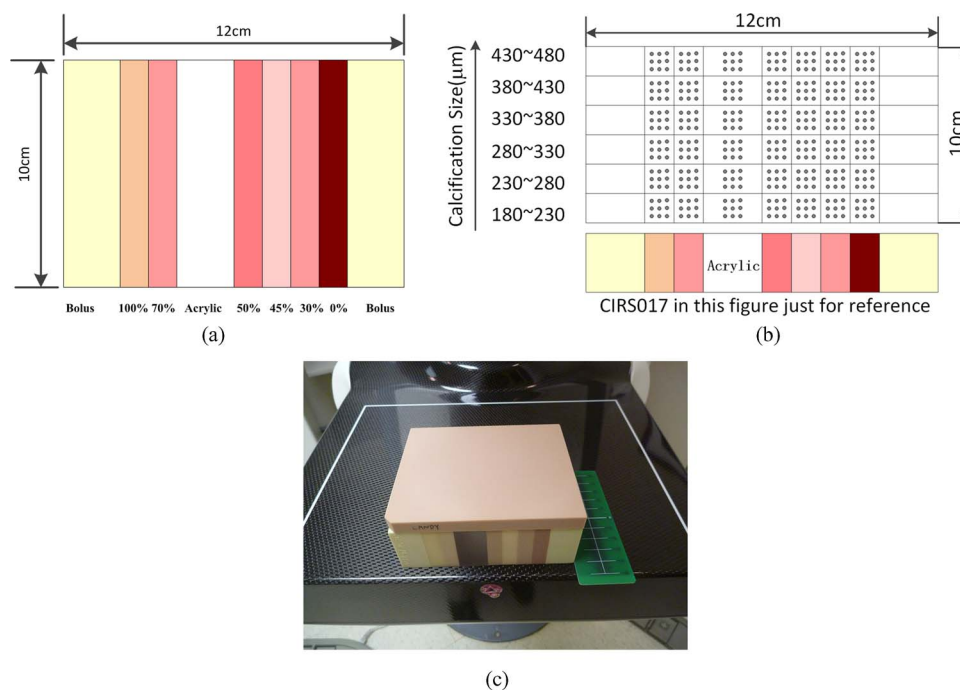


FIG. 2. (a) Schematic drawing of the breast phantom (Model 017). (b) The calcification phantom consisting of 42 calcification clusters ( $\text{Al}_2\text{O}_3$  crystals) arranged in a  $6 \times 7$  grid. Each cluster consisted of nine calcifications in a  $3 \times 3$  pattern. The clusters were arranged by size into six rows with nominal size ranges of 180–230, 230–280, 280–330, 330–380, 380–430, and 430–480  $\mu\text{m}$ . (c) Imaged object. Calcification phantoms lay on the breast phantom CIRS Model 017.

$12 \times 10 \times 1 \text{ cm}^3$  (length  $\times$  width  $\times$  height). The imaged object was constructed by placing the calcification phantom on the breast phantom [Fig. 2(c)]. The combination resulted in a rectangular slab of 5 cm fixed thickness with varying glandular ratio and fixed calcification size along the longer side and fixed glandular ratio and varying calcification size along the shorter side.

### 3.C. Calibration measurement and inverse-map function

As we mentioned in Sec. 2.A, Eq. (4) was used to do DEDM calculation. The coefficients  $a_m$  and  $b_n$  ( $m = 0, \dots, 9$ ;  $n = 0, \dots, 4$ ) should be predetermined from separately acquired calibration data. When we use different materials for calibration measurement and imaging, the attenuation differences between imaged object and calibration phantoms can yield large calculation errors.<sup>21,22</sup> In order to investigate the scatter correction method independently, we used the same breast phantom for both calibration measurement and imaging. Because of the difficulty in making calcifications with accurate size for quantitative calibration measurements, a mammographic aluminum stepwedge (Model 118, GMMEX Inc., Middleton, WI) was used to simulate x-ray attenuation of calcifications for calibration measurement. The wedge was 1.5 cm wide, 11.5 cm long, and had 9 steps, each 250  $\mu\text{m}$  higher than the previous step; the copper backing strip and the plastic coating were removed during measurement. The calibration measurement was performed at five glandular ratios (0%, 30%, 50%, 70%, and 100%) of the 5-cm-thick phantoms with five aluminum thicknesses (0, 250, 500, 750, 1000  $\mu\text{m}$ ). In order to reduce the statistical uncertainties

of the calibration measurements, the mAs values were increased. For the calibration procedure, a mammographic x-ray tube was used with a rhodium (Rh) anode and Rh filter, using technique equal to 100 mAs at 28 kVp and 16 mAs at 48 kVp, for the LE and HE images, respectively. It can be observed that the mAs used for calibration are higher than those for imaging but much lower than 28 kVp at 320 mAs and 49 kVp at 22.5 mAs used by Kappadath and Shaw.<sup>15</sup> We also measured the variance in the DE images for different mAs values: 50, 100, 200, and 320 mAs at 28 kVp and 12.5, 16, 18, and 22.5 mAs at 48 kVp. The results indicated that the uncertainties had no obvious decrease when mAs were increased higher than 100 mAs at 28 kVp and 16 mAs at 48 kVp in our digital mammography system. In order to avoid the high tube loading, we used 100 mAs at 28 kVp and 16 mAs at 48 kVp for the calibration measurement.

The calibration measurement was carried out under narrow-beam geometry as shown in Fig. 3. The x-ray beam was defined by a precollimator on the tube side of the phantom and by a postcollimator on the breast support. Each collimator was a 1-mm-thick lead sheet with a 5 mm diameter hole. The two collimators were carefully aligned. The average value of the central  $11 \times 11$  pixels in the collimator area was used as calibration data. We have verified by Monte Carlo simulation<sup>32,33</sup> that a very small amount of scatter (1.6% for LE images and 1.5% for HE images) was present in the central  $11 \times 11$  pixels. The signals for 0% glandular ratio were selected as the reference signals  $I_{rl}$  and  $I_{rh}$ . The coefficients of Eq. (4) were estimated using a nonlinear least-squares fitting to the calibration data. By investigating the residuals of the fit, we can give a practical estimate of the fitting accuracy of the inverse function Eq. (4). The residuals are defined as the

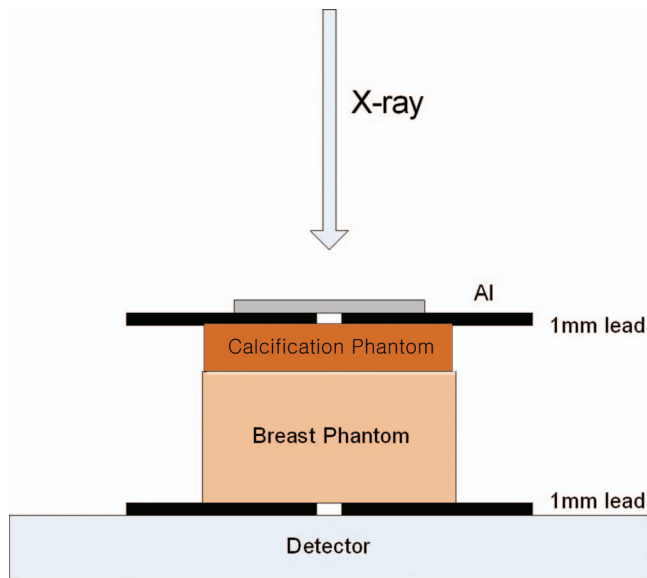


FIG. 3. Schematic of the calibration measurements under narrow-beam geometry.

difference between the true calibration value and the value returned by the fit. Specifically, the median, the root-mean-square (rms), and the maximum absolute deviation (max) values, computed from the distribution of residual values were used to compare and evaluate the goodness of fit. The median, rms, and maximum of the fitting residuals were  $-2$ ,  $17$ , and  $45 \mu\text{m}$ , respectively.

### 3.D. Reference Images for nonuniformity correction

The mammography system automatically corrects for gain nonuniformities, defective pixels, and dark current noise (offset) in every raw image acquired. However, these corrections were largely independent of the kVp, mAs, and the imaged object. Image nonuniformity varies with x-ray energy and leads to errors in computing the signal  $D_j$  ( $j = l, h$ ) [Eq. (3)] and the DE calcification image  $t_c$  [Eq. (4)]. In order to correct the spatial nonuniformity together with the beam hardening effects more accurately, we adopted the method suggested by Kappadath and Shaw.<sup>15</sup> A 5-cm-thick Lucite phantom was imaged at 28 kVp/50 mAs (5 times) and 48 kVp/12.5 mAs (5 times). The reference LE or HE image generated was an average of the five images separately acquired to minimize the random noise fluctuations. Additionally, the reference image was filtered by a low-pass filter (boxcar) with the kernel size of  $31 \times 31$  pixels to further reduce the noise. When computing  $D_j$  for each pixel in the LE or HE image, we used the pixel values on the corresponding locations in the reference image as the reference signal  $I_{rj}$ .

### 3.E. Measurement of primary, scattered radiations and SPRs

To verify the scatter correction method proposed in this study, the primary and scattered radiations were experimentally determined. Various methods have been investigated

and implemented to measure the scatter component in image signals, including the beam stop, slit, edge spread, and pinhole-array interpolation methods. In this study, we used the pinhole-array interpolation method.<sup>15,27</sup> With this method, a 3-mm-thick lead sheet with pinhole-array was placed underneath the breast phantom for imaging. The lead sheet consisted of a 2D array of pinholes, each 1 mm in diameter and space 1 cm apart, center to center, vertically, and horizontally. In the LE and HE phantom images acquired with the lead sheet in place, the radiations in the aperture areas were mostly primary signals. The signals outside the aperture were almost zero. The LE and HE phantom images acquired without the lead sheet in place contained both the primary and scattered radiation. In practice, when acquiring images without lead sheet, a 3-mm-thick acrylic sheet with an  $11.7 \times 9.7 \text{ cm}^2$  rectangular hole replaced the lead sheet. Therefore, a 3 mm air-gap was between the phantom and the breast support and the distance from the phantom to the focal spot was fixed with or without the lead sheet. The images acquired with the lead sheet may be subtracted from those acquired without the lead sheet to estimate the scatter component in the aperture areas. For each pinhole, signals in a  $2 \times 2$  pixels region at the center were averaged and used to estimate the primary signal,  $\tilde{P}(x, y)$ , and the primary plus scatter signal,  $I'(x, y)$ , at the aperture center,  $(x, y)$ . In fact,  $\tilde{P}(x, y)$  is only an approximation for the real primary signal  $P(x, y)$ . Thus, the scatter component,  $S(x, y)$ , may be estimated by subtracting the two signals as follows:

$$S(x, y) = I'(x, y) - P(x, y) \approx I'(x, y) - \tilde{P}(x, y). \quad (9)$$

The scatter signal in the entire full-field image can be estimated by cubic spline interpolating between the spot estimates of scatter. Once the primary and scatter signals were estimated, the SPR may be computed as follows:

$$\text{SPR}(x, y) = \frac{S(x, y)}{\tilde{P}(x, y)}. \quad (10)$$

The pinhole-array interpolation method was proved to be effective in scatter measurement.<sup>27</sup> In this paper, the accuracy of this method was evaluated by Monte Carlo simulations.<sup>34,35</sup> When a 1-mm diameter pinhole lead sheet (3-mm-thick) was placed underneath the object, the in-hole scatter fraction ( $2 \times 2$  central pixels region) was 1.8% for LE image or 1.3% for HE image; the crosstalk was estimated to be zero. Therefore, placing the lead sheet (1 mm diameter pinhole) underneath the object is acceptable and corresponding to an overestimation of the primary signal by about 1.8% (LE) and 1.3% (HE) in our study.

### 3.F. Evaluation of the DE calcification images

Three DE calcification images were computed in this study: DE image with scatter correction using our algorithmic method, DE image with scatter correction using pinhole-array interpolation method, and DE image without scatter correction.

First, we constructed the LE and HE reference images. Next, the LE and HE images of the imaged object with the

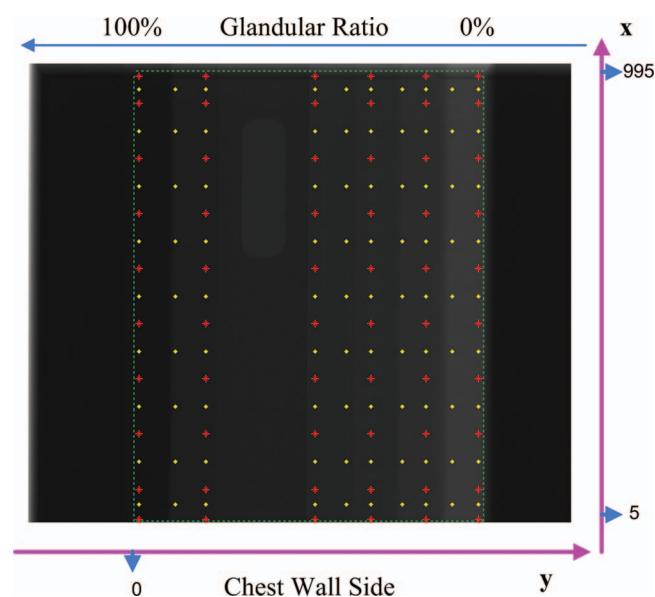


FIG. 4. High energy image of breast phantom, the region inside the green dashed lines is  $1000 \times 800$  pixels, asterisks indicate independent pixels, and dots indicate dependent pixels in algorithmic scatter correction method.

pinhole-array lead sheet were acquired. The LE and HE images of the imaged object were then acquired. Since the phantom imaged had physical dimensions of  $12 \times 10 \times 4 \text{ cm}^3$  with  $2 \times 10 \times 4 \text{ cm}^3$  water equivalent bolus on each end, the acquired images were trimmed and only  $1000 \times 800$  pixels were kept (Fig. 4).

As mentioned in Sec. 2.C, we sampled  $N$  pixels in the LE phantom image and the corresponding  $N$  pixels in the HE image, including  $k_1$  (asterisks) independent pixel pairs and  $k_2$  (dots) dependent pixel pairs. We did not sample pixels in the acrylic area. Pixel values of the same locations in the reference images were selected. Therefore, we constructed an equation set with  $N$  equations. [Each one was Eq. (4) and  $t_c$  was forced to zero.] and  $2k_1$  unknowns  $S_{ij}$  ( $i = 1, \dots, k_1; j = l, h$ ). A least-squares algorithm was employed to estimate  $S_{ij}$ . Using these  $S_{ij}$  of the sampled pixels we generated an estimate of scatter field by cubic spline interpolation and then subtracting it from the phantom image. Thus the scatter corrected LE and HE images were computed. Substituting the scatter corrected  $D_j$  ( $j = l, h$ ) signals into Eq. (4), we generated the DE calcification image.

The scatter in the LE and HE phantom images were also estimated and corrected using the pinhole-array interpolation method. The DE calcification image was built. The DE calcification image was also constructed without scatter correction of the phantom images.

### 3.F.1. Background DE calcification signal

Ideally, the DE calcification image signal  $t_c$  would fluctuate around zero if there was no calcification in the phantom. Such calcification image signal was referred to as background DE calcification signal. We compared the  $t_c$  values of selected pixels in the three DE calcification images. However, the

individual pixel values were susceptible to image noise fluctuations, so the median and rms values in 25 regions-of-interest (ROI) of size  $31 \times 31$  pixels each distributed in a  $5 \times 5$  grid across the image were also computed to estimate the background DE calcification signal and noise fluctuations. ROIs were selected in the regions of glandular ratios 0%, 30%, 45%, 50%, and 70%. The differences in the median, rms, and range of the background DE calcification signals between the three DE calcification images were used to evaluate the effects of scatter correction.

### 3.F.2. Calcification CNRs

We performed a simple visual evaluation of the calcifications in this paper. First, the ensemble average of five LE images was used to determine the pixel locations of the calcifications in the image. And then, the CNR of each calcification in the DE calcification images was calculated:<sup>36</sup>

$$\text{CNR} = \frac{|S_{\mu c} - S_B|}{\sigma} \times \sqrt{A}, \quad (11)$$

where  $S_{\mu c}$  is the mean signal for each calcification which was determined by averaging the calcification signal over the pixels corresponding to that calcification size.  $S_B$  and  $\sigma$  are the mean and variance of the background (zero calcification) signal, respectively, of a  $61 \times 61$  pixel region in the image adjacent to each of the calcification clusters.  $A$  is the area of calcification in the DE image. In this experiment, a 5MP diagnostic display system (Nio 5MP, Barco Inc., Duluth, GA, USA) was used with a pixel pitch is 0.1650 mm.

We evaluated the effectiveness of the scatter correction techniques by directly comparing the CNR (or visibility) of the three calcification sizes (230–280, 280–330, and 330–380  $\mu\text{m}$ ) in the DE calcification images. The CNR threshold for calcification visibility was 1.0. The CNR threshold is determined by a simple visual inspection. Two people read five LE images and five HE images on a 5MP (Nio 5MP, Barco Inc., Duluth, GA, USA) diagnostic display system and gave the estimation.

## 4. RESULTS

### 4.A. Background DE calcification signal

As illustrated in Fig. 4, we sampled 150 pixels in the LE phantom image and the corresponding 150 pixels in the HE image, including 60 independent pixel pairs and 90 dependent pixel pairs. Independent pixel pairs were sampled from pixel number 5 to pixel number 995, and hence, 12 independent pixel pairs were selected across the length of the phantom. A smaller sampling interval was used near the edge of the phantom where the scatter profiles change relatively faster. The sampling interval (between independent pixels) was approximately 60 pixels close to the edge. Sampling distance in the other direction was about 120 pixels. The SPRs measured by the pinhole-array interpolation method and algorithmic method at the same locations are listed in Tables I and II. SPR ranged from 17% to 67% in the LE image and from 18% to 48% in the HE image without scatter

TABLE I. SPRs measured by the algorithmic method (bold) and pinhole-array interpolation method at the same locations with different glandular ratios in phantoms, low energy.

Glandular (%)		SPR (%)								
0	<b>19.9</b>	<b>24.1</b>	<b>23.1</b>	<b>23.8</b>	<b>22.6</b>	<b>25.9</b>	<b>26.7</b>	<b>27.4</b>	<b>28.1</b>	<b>32.5</b>
	19.0	20.0	21.0	18.2	17.0	19.6	19.7	20.7	20.7	31.5
30	<b>20.9</b>	<b>23.5</b>	<b>21.6</b>	<b>24.8</b>	<b>25.4</b>	<b>27.9</b>	<b>26.7</b>	<b>28.0</b>	<b>29.2</b>	<b>32.2</b>
	20.4	18.8	18.2	19.1	19.2	23.9	18.2	24.5	20.5	30.3
45	<b>21.1</b>	<b>21.4</b>	<b>21.4</b>	<b>22.1</b>	<b>23.6</b>	<b>21.5</b>	<b>25.2</b>	<b>26.4</b>	<b>24.1</b>	<b>38.2</b>
	21.4	19.2	17.6	18.8	19.2	17.0	18.7	22.9	15.9	31.7
50	<b>21.9</b>	<b>21.5</b>	<b>24.2</b>	<b>23.8</b>	<b>26.4</b>	<b>32.2</b>	<b>31.1</b>	<b>26.1</b>	<b>29.4</b>	<b>38.5</b>
	21.9	18.1	19.5	18.9	21.1	19.5	32.5	19.3	20.6	32.8
70	<b>25.4</b>	<b>23.5</b>	<b>19.2</b>	<b>19.9</b>	<b>24.7</b>	<b>25.8</b>	<b>29.3</b>	<b>28.9</b>	<b>31.6</b>	<b>40.1</b>
	27.6	20.0	19.9	20.9	22.9	23.2	22.9	26.5	34.6	39.2
100	<b>21.7</b>	<b>23.4</b>	<b>22.9</b>	<b>20.9</b>	<b>29.0</b>	<b>26.1</b>	<b>23.9</b>	<b>39.5</b>	<b>38.1</b>	<b>67.8</b>
	25.3	25.8	23.9	20.9	25.9	25.6	27.5	28.0	24.5	62.5

correction for the different glandular ratios. The mean value of SPR estimated using algorithmic method was about 26.7% for the LE image, 26.9% for the HE image. The mean value of SPR estimated using pinhole-array interpolation method was about 23.2% for the LE image, 24.7% for the HE image. The surface plots of the scatter signal estimated using this algorithmic method and pinhole-array interpolation method for LE and HE images are shown in Fig. 5. The shapes of estimated scatter fields using the two different methods looked similar. The scatter fields estimated using the algorithmic method seems to be smoother than the scatter field estimated using the pinhole-array interpolation method.

Figures 6(a) and 6(b) show the difference of SPRs estimated by algorithmic method and pinhole-array method:

$$\text{SPR}_d = \text{SPR}_{\text{algorithm}} - \text{SPR}_{\text{pinhole-array}}. \quad (12)$$

The differences ranged from  $-3.6\%$  to  $13.6\%$  for the LE image, and from  $-4.0\%$  to  $8.3\%$  for the HE image. The biggest difference was found in the LE image for the 100% glandular ratio tissue equivalent material, which was due to the reduced number of photons and thus an increased sensitivity to photon noise.

We also implemented the experiment with the breast phantom Model017 (4-cm-thick) only. SPR ranged from 11% to 39% in the LE image and from 13% to 40% in the HE image without scatter correction. The mean value of SPR estimated using algorithmic method was approximately 19.2% for the LE image, and approximately 21.3% for the HE image. The mean value of SPR estimated using pinhole-array interpolation method was about 16.8% for the LE image, and 18.9% for the HE image. Figures 6(c) and 6(d) show the difference of SPRs estimated by algorithmic method and pinhole-array method for the 4-cm-thick breast phantom. The differences ranged from  $-5.0\%$  to  $13.0\%$  for LE image, and from  $-1.8\%$  to  $10.8\%$  for HE image.

After the scatter correction of LE and HE images, the DE calcification images were calculated. (The following results were based on the calcification phantom and breast phantom together.) There are 60 background DE calcification signals  $t_c$  presented in Table III, which came from the calcification image calculated based on the pinhole-array interpolation scatter correction. These corresponding 60 pixel pairs lay at the locations of the center of pinholes. We also adopted these pixels pairs as independent pairs and estimated their scatter signal  $S_{ij}$  ( $i = 1, \dots, 60; j = l, h$ ) using our algorithmic method.

TABLE II. SPRs measured by the algorithmic method (bold) and pinhole-array interpolation method at the same locations with different glandular ratios in phantoms, high energy.

Glandular (%)		SPR (%)								
0	<b>19.6</b>	<b>24.2</b>	<b>24.4</b>	<b>24.6</b>	<b>23.4</b>	<b>24.5</b>	<b>24.4</b>	<b>25.0</b>	<b>26.3</b>	<b>27.4</b>
	18.1	23.9	23.6	21.2	19.5	21.2	20.4	21.7	22.4	27.9
30	<b>21.4</b>	<b>22.7</b>	<b>23.7</b>	<b>24.8</b>	<b>25.0</b>	<b>28.1</b>	<b>25.6</b>	<b>27.1</b>	<b>27.6</b>	<b>30.9</b>
	19.9	19.7	21.5	21.8	21.3	26.3	21.9	25.9	22.6	30.0
45	<b>21.9</b>	<b>22.6</b>	<b>23.8</b>	<b>23.8</b>	<b>26.9</b>	<b>24.3</b>	<b>26.6</b>	<b>26.5</b>	<b>26.6</b>	<b>31.4</b>
	21.7	21.3	21.8	21.8	24.2	21.7	22.0	24.5	22.0	29.3
50	<b>23.0</b>	<b>22.8</b>	<b>24.7</b>	<b>24.5</b>	<b>25.3</b>	<b>31.2</b>	<b>31.4</b>	<b>25.6</b>	<b>27.4</b>	<b>31.3</b>
	22.7	20.6	23.6	22.6	23.9	22.9	33.2	22.7	23.1	29.1
70	<b>25.1</b>	<b>26.6</b>	<b>23.9</b>	<b>23.5</b>	<b>27.5</b>	<b>26.8</b>	<b>30.2</b>	<b>30.1</b>	<b>26.2</b>	<b>31.6</b>
	23.8	21.1	23.1	23.2	26.9	25.9	26.7	30.4	30.2	32.1
100	<b>25.8</b>	<b>27.3</b>	<b>27.3</b>	<b>26.7</b>	<b>31.1</b>	<b>30.3</b>	<b>28.7</b>	<b>35.7</b>	<b>33.2</b>	<b>47.1</b>
	26.0	27.3	27.7	23.8	30.3	27.9	27.9	32.1	26.2	46.3

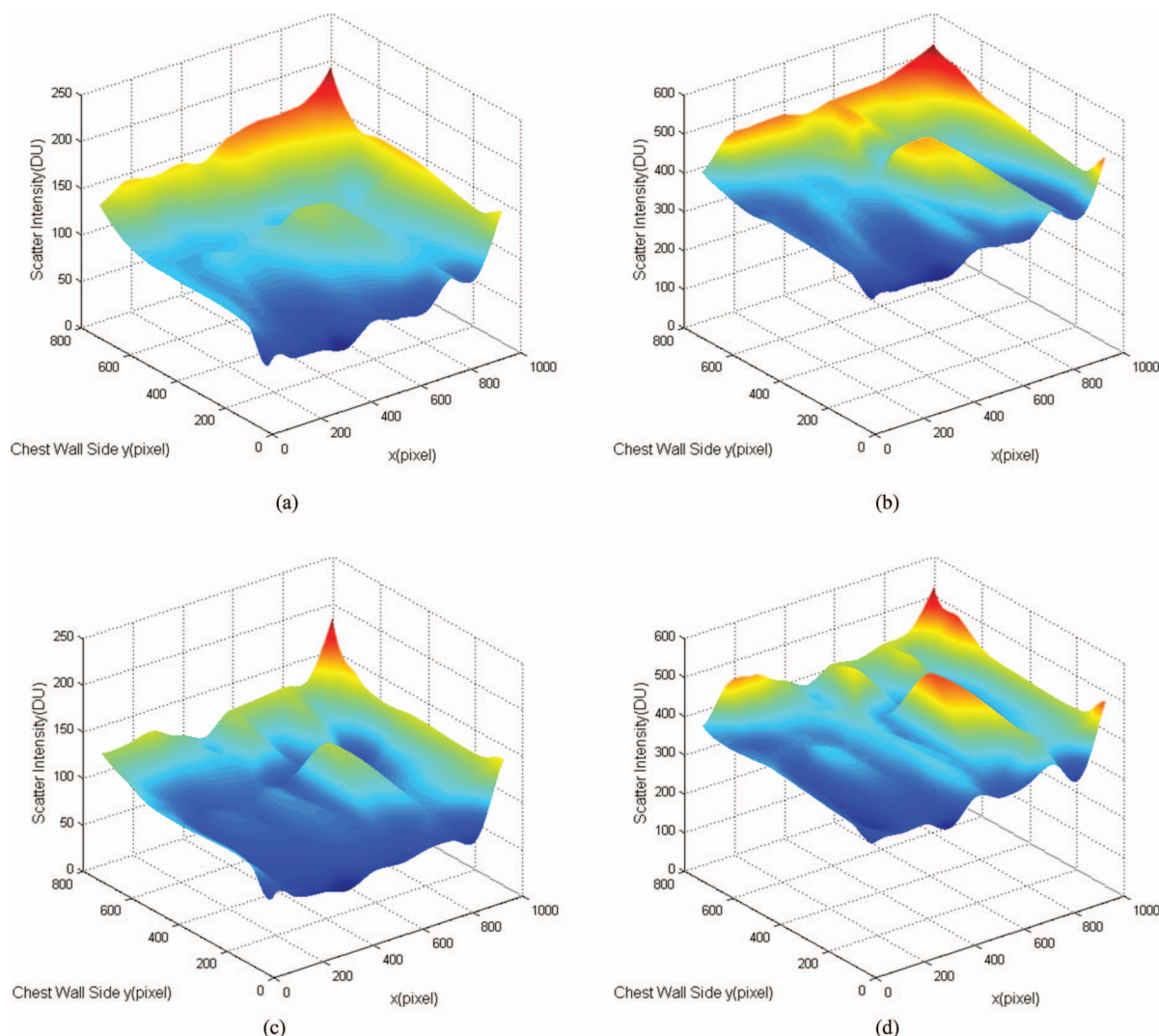


FIG. 5. Scatter signal field estimated using the algorithmic method and pinhole-array interpolation method: (a) algorithmic method LE, (b) algorithmic method HE, (c) pinhole-array interpolation method LE, and (d) pinhole-array interpolation method HE.

The resultant background DE calcification signals  $t_c$  are listed in Table IV. The background DE calcification signals  $t_c$  calculated without scatter correction are listed in Table V. The background DE calcification signals calculated based on the pinhole-array interpolation scatter correction method (Table III) were somewhat nonuniform (median  $-58 \mu\text{m}$ , rms  $229 \mu\text{m}$ , and range  $968 \mu\text{m}$ ). The calcification thickness calculated based on the algorithmic scatter correction method (Table IV) yielded a distribution of median  $4 \mu\text{m}$ , rms  $93 \mu\text{m}$ , and range  $306 \mu\text{m}$  of background signals. In contrast, the calcification thickness computed without scatter correction (Table V) yielded a distribution of median  $1962 \mu\text{m}$ , rms  $1920 \mu\text{m}$ , and range  $888 \mu\text{m}$  of background signals.

The median, minimum, and maximum background signals of the  $5 \times 5$  array of ROI in the DE calcification image, using scatter corrected (algorithmic method and pinhole-array interpolation method) and uncorrected LE and HE images are listed in Table VI. We observed reduced background DE calcification signal after scatter correction, both scatter correction techniques were effective. However, the reduction was

more pronounced using the algorithmic method rather than the pinhole-array interpolation method for scatter correction. The rms of background DE calcification signal of  $1962 \mu\text{m}$  with scatter-uncorrected data was reduced to  $194$  and  $384 \mu\text{m}$  after scatter correction, using our algorithmic method and pinhole-array interpolation method, respectively. According to the minimum and maximum values of the ROI signal listed in Table VI, the range of background DE calcification signals can be estimated. The range of background signals using scatter-uncorrected data was  $593 \mu\text{m}$ . After scatter correction using our algorithmic method, the range was reduced to  $251 \mu\text{m}$ . The range was reduced by 58%.

The results of algorithmic scatter correction method listed above were all acquired with sampling interval  $60$ – $120$  pixels as illustrated in Fig. 4. Table VII lists the median, minimum, and maximum background signals in the  $5 \times 5$  array of ROI when the algorithmic scatter correction method was applied with different sampling intervals. If uniform sampling (sampling interval kept the same across the whole image) was used and the sampling interval was reduced to  $50$  pixels, similar

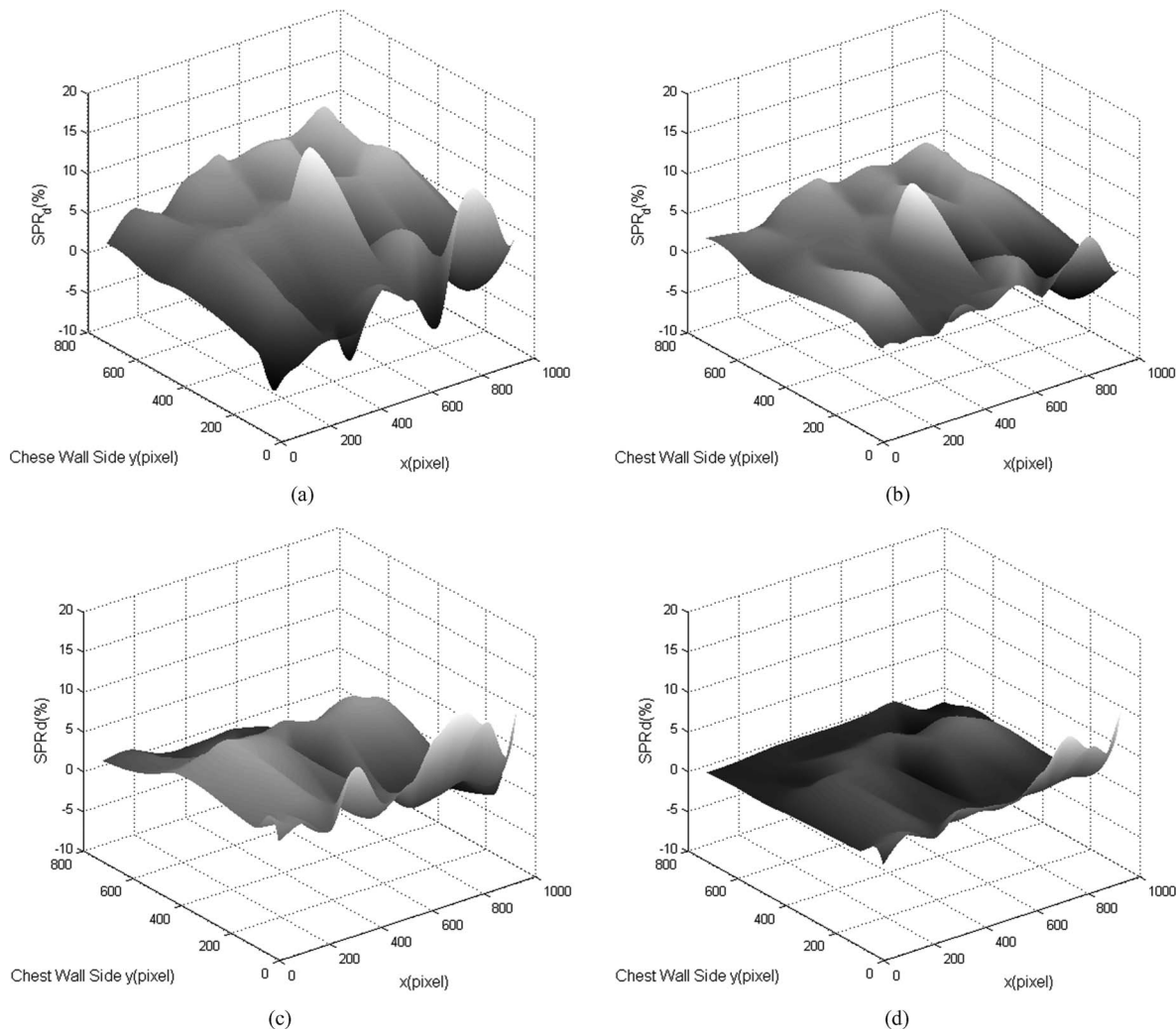


FIG. 6. The differences of SPRs estimated by algorithmic method and pinhole-array method: (a) LE (5 cm thick), (b) HE (5 cm thick), (c) LE (4 cm thick), and (d) HE (4 cm thick).

TABLE III. Background DE calcification signals calculated based on the pinhole-array interpolation scatter correction, the 60 pixel pairs lay on the locations of the center of pinholes.

Glandular (%)		Background DE calcification signal $t_c$ ( $\mu\text{m}$ )								
0	338	-298	-194	-145	12	-247	-118	-206	-260	-282
30	232	91	-61	-488	-32	-188	-56	-267	-137	-174
45	219	47	82	148	-79	61	76	-106	-194	-204
50	171	126	-25	195	-49	-83	-226	-139	-112	-249
70	463	464	300	284	61	-111	34	-353	-289	-155
100	265	354	-36	480	-49	397	469	-126	-159	-241

TABLE IV. Background DE calcification signals calculated based on algorithmic scatter correction, the pixel pairs were independent pairs in algorithmic method.

Glandular (%)		Background DE calcification signal $t_c$ ( $\mu\text{m}$ )								
0	126	159	-87	-103	-61	-120	-42	-35	-106	-72
30	133	74	-78	91	44	-46	145	-103	-32	-118
45	152	55	144	151	-76	93	-57	-78	-97	-4
50	118	105	143	72	152	-39	1	139	-30	7
70	102	9	130	160	12	27	89	-146	107	48
100	-98	-66	-34	-46	25	-23	-18	120	-74	-64

TABLE V. Background DE calcification signals without scatter correction, pixel pairs were the same as in Tables III and IV.

Glandular (%)	Background DE calcification signal $t_c$ ( $\mu\text{m}$ )									
0	1766	2197	2123	2038	2001	1725	1687	1738	1832	1526
30	1797	1800	1939	2018	1975	2024	2010	1815	1834	2048
45	1921	1878	2152	2084	2141	2191	2044	1801	2025	1673
50	1957	1913	1997	1923	1885	1966	2091	1940	1766	1462
70	1790	2010	2135	2049	2052	1876	2101	1925	1309	1411
100	1865	2001	2020	2092	2067	2085	2116	2032	1547	1432

equations in the equation set were generated which led to a singular matrix. We could not get any results. If nonuniform sampling interval 50–70 pixels was used (50 pixels near the edge and 70 pixels in the central part of the image), the scatter fields [Figs. 7(a) and 7(b)] can be acquired, but have more fluctuations, not being as smooth as those in Fig. 5, especially for the HE image. The background DE calcification signals were not as smooth as those acquired with sampling interval 60–120 pixels. When sampling interval was increased to 150 pixels (uniform sampling), the results are worse than those with sampling interval 60–120 pixels. The median ROI rms was increased from 194 to 336  $\mu\text{m}$ . When sampling interval was increased to 180–210 pixels (180 pixels near the edge and 210 pixels in the central part of the image), the results deteriorated. Scatter estimates could not be acceptable [Figs. 7(c) and 7(d)] and big values of background DE calcification signals in ROIs were observed. From the results listed in Table VII, considering the computation load and scatter fractions change faster near the edge than in the central part of the image, we selected 60 pixels sampling interval near the edge and 120 pixels sampling interval in the central part of the image.

DEDM is an imaging technique whose resultant calcification signal is sensitive to image noise in LE and HE images. And hence, noise reduction techniques have been investigated to counteract the increase in DE calcification signal noise.<sup>17</sup> In this study, a median filter (kernel = 5) was applied to the HE image prior to scatter correction and computation of the DE image. The results are listed in Table VIII, and the sampling interval remained 60–120 pixels. Noise reduction technique influenced and reduced the background DE calcification signals in the ROIs. The range of ROI signal was reduced from 251 to 198  $\mu\text{m}$  and the median of ROI rms was reduced from 194 to 153  $\mu\text{m}$ .

#### 4.B. Calcification CNRs

Figure 8 shows a section of LE and DE calcification images without any adjustment of the image brightness and contrast. The image section corresponds to a glandular ratio of 30% with calcification sizes of 180–230 (left), 230–280, 280–330, 330–380, and 380–430  $\mu\text{m}$  (right). Four images were shown: DE calcification image without scatter correction (DE/o), DE calcification with pinhole interpolation scatter correction (DE-pin), DE calcification with algorithmic scatter correction (DE-al), and DE calcification with algorithmic scatter correction and HE median filtered (DE-al-de). If scatter correction was not carried out, only some calcifications with size 380–430  $\mu\text{m}$  were visible in DE calcification image [Fig. 8(a)]. After scatter correction, the visible calcification size can be reduced to 280–330  $\mu\text{m}$  [Figs. 8(b)–8(d)].

According to Eq. (11), the CNRs of the calcifications were computed for DE calcification images without/with scatter correction. Table IX shows the direct comparison of the average calcification CNR of the three calcification clusters (230–280, 280–330, and 330–380  $\mu\text{m}$ ) over three glandular ratios of 30%, 45%, and 70% in the DE calcification images to evaluate the effectiveness of the scatter correction techniques. Since each calcification cluster contains nine calcifications, the average CNR is the mean value of the nine CNRs.

An approximate CNR threshold for calcification visibility was estimated to be approximately 1.0. As seen in Fig. 8(c), calcifications greater than 330  $\mu\text{m}$ , that yielded an average CNR value of 1.47, were clearly visible in the DE calcification image with algorithmic scatter correction; while most of 280–330  $\mu\text{m}$  calcifications and only some of the 230–280  $\mu\text{m}$  calcifications with CNR values of 1.0 and 0.67, respectively, were visible in the DE calcification images [Fig. 8(c)].

TABLE VI. The median, minimum, and maximum background DE calcification signals ( $\mu\text{m}$ ) in the regions-of-interest with and without scatter correction.

DE calcification image	ROI signal ( $\mu\text{m}$ )			ROI rms ( $\mu\text{m}$ )		
	Median	Min	Max	Median	Min	Max
Algorithmic method scatter correction	15	−127	124	194	30	785
Pinhole-array interpolation method scatter correction	−10	−252	355	384	69	864
Without scatter correction	1953	1489	2082	1962	1557	2087

TABLE VII. The median, minimum, and maximum background DE calcification signals ( $\mu\text{m}$ ) in the regions-of-interest when the algorithmic method was used with different sampling intervals.

Sampling interval (pixels)	ROI signal ( $\mu\text{m}$ )			ROI rms ( $\mu\text{m}$ )		
	Median	Min	Max	Median	Min	Max
50	Singular matrix					
50–70	–4	–135	167	285	34	816
60–120	15	–127	124	194	30	785
150	38	–182	233	336	33	873
180–210	162	–198	326	391	67	1264

As can be seen in Table IX, calcifications below  $380\ \mu\text{m}$  were invisible in DE calcification image without scatter correction. Both scatter correction techniques were effective, algorithmic scatter correction method is better since the CNR with this method is a little higher than CNR with pinhole interpolation method. If we used denoised techniques, the CNR can be improved. After denoising, some calcifications of size

TABLE VIII. The median, minimum, and maximum background DE calcification signals ( $\mu\text{m}$ ) in the regions-of-interest when algorithmic method was used with and without denoising technique. Sampling interval was 60–120 pixels.

Denoising	ROI signal ( $\mu\text{m}$ )			ROI rms ( $\mu\text{m}$ )		
	Median	Min	Max	Median	Min	Max
No	15	–127	124	194	30	785
Yes	5	–97	101	153	35	731

$230\text{--}280\ \mu\text{m}$  were visible with average CNR values greater than 1 (in glandular 45% and 70% of Table IX).

## 5. DISCUSSION

### 5.A. Background DE calcification signal

In this paper, we investigated the accuracy of an algorithmic scatter correction method. The scatter intensity fields (Fig. 5) estimated using this algorithmic method and the

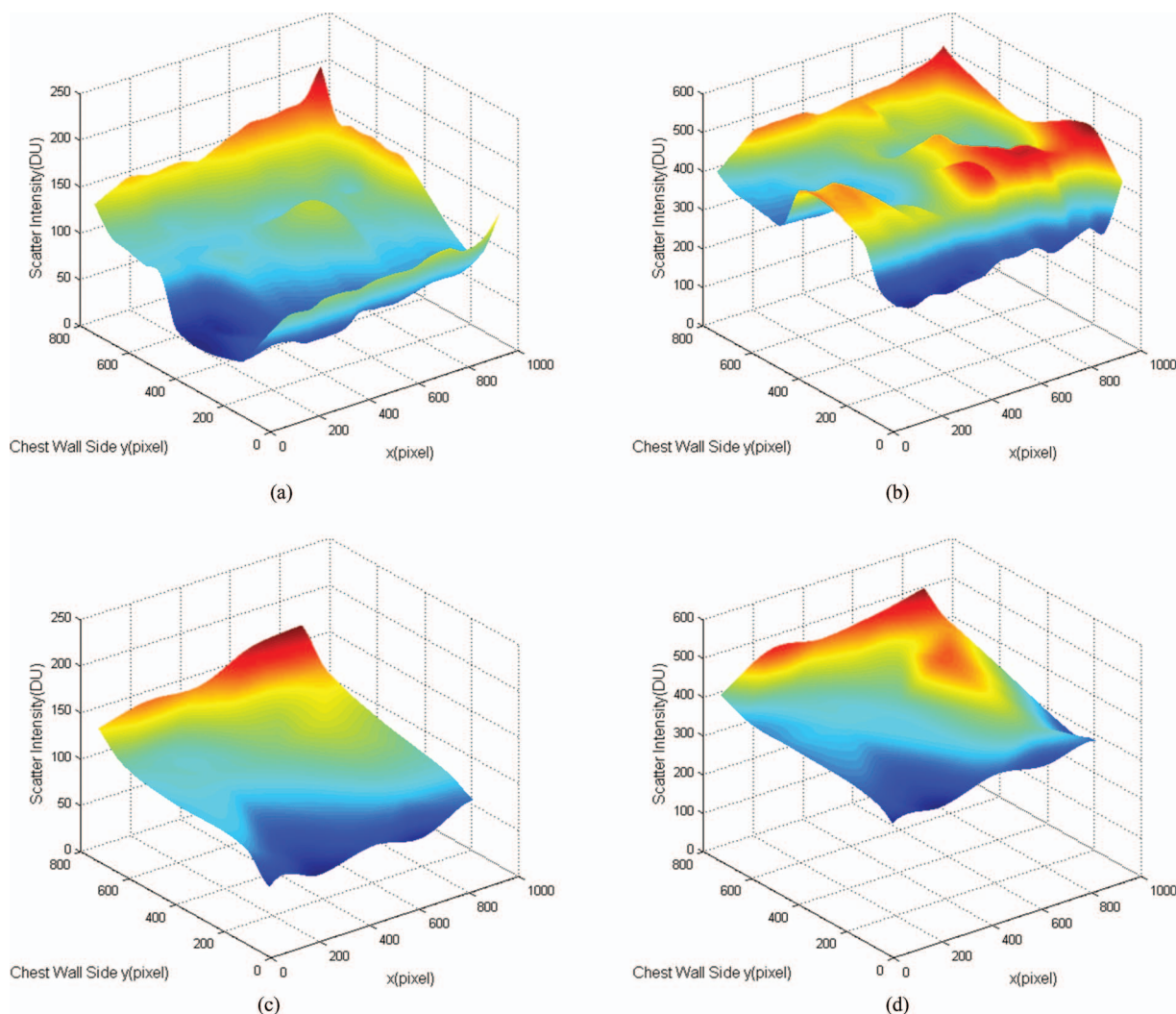


FIG. 7. Scatter signal field estimated using the algorithmic method: (a) sampling interval 50–70 pixels, LE, (b) sampling interval 50–70 pixels, HE, (c) sampling interval 180–210 pixels, LE, and (d) sampling interval 180–210 pixels, HE.

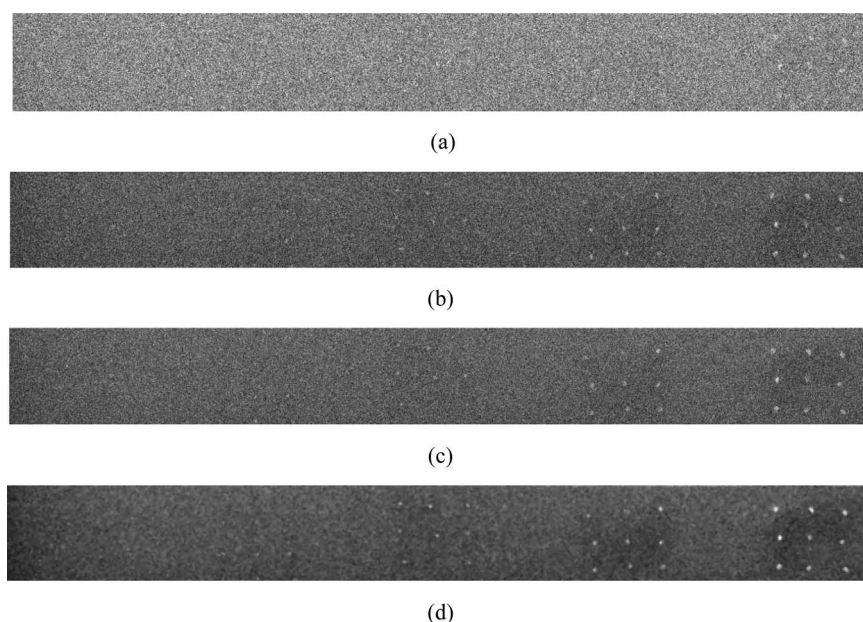


FIG. 8. A  $80 \times 865$  pixel corresponding section of the LE and DE calcification images (1643–1722, 68–932) showing calcification size ranges of 180–230 (left), 230–280, 280–330, 330–380, and 380–430  $\mu\text{m}$  (right) for 30% glandularity tissue-equivalent material data. (a) DE/o, (b) DE-pin, (c) DE-al, and (d) DE-al-de.

pinhole-array interpolation method for both LE and HE images looked similar. Our results indicate that the background DE calcification signals without scatter correction are very large with median value of 1953  $\mu\text{m}$  in the ROI (Table VI). Scatter correction can reduce the magnitude of background DE calcification signals. Using our algorithmic scatter correction method, the median background DE calcification signal can be reduced to 15  $\mu\text{m}$ , and the range of background DE calcification signals can be reduced by approximately 58%. The background DE calcification signals yielded a uniform distribution after scatter correction. So the scatter correction method proposed here is effective.

In this study, we also implemented pinhole-array interpolation method to measure scattered radiations. As listed

in Tables I and II and shown in Figs. 5 and 6, the differences were not big between scatter estimated with algorithmic method and scatter measured with pinhole-array interpolation method. The differences between the two methods for the 4-cm-thick phantom were smaller in magnitude than the difference between the methods for the 5-cm-thick phantom, since scatter fraction increases with increasing patient thickness. The average difference for both phantoms is no more than 4%. So the scatter correction method proposed here is effective for different breast phantom thicknesses.

The polynomial fitting errors and quantum noise both contributed to the differences of scatter estimation between the two methods. As listed in Table VI, when using the pinhole-array interpolation method, the median value of the ROI signal is  $-10 \mu\text{m}$  and the ROI rms is 384  $\mu\text{m}$ , which agreed with the results in Kappadath and Shaw's experiment.<sup>15</sup> Compared to the median values of the ROI signal (1953  $\mu\text{m}$ ) and rms (1962  $\mu\text{m}$ ) without scatter correction, both methods appeared to be effective and have comparable ability in scatter correction; however, the algorithmic method achieved slightly smaller background DE calcification signals than the pinhole-array interpolation method. The main reason is that when using the algorithmic method, the scatter of the sampled pixels was estimated by an equation set with more than 100 equations, so the noise in the sampled pixels was suppressed to some extent. However, when using pinhole-array interpolation method, the scatter signal in the entire full-field image was estimated by interpolating between the spot estimates of scatter which is sensitive to fluctuations in the spot measurements. Therefore, there was bigger variation in the background DE calcification signals when using pinhole-array interpolation method. Kappadath and Shaw<sup>15</sup> adopted an analytical model to describe the scatter field, which is less sensitive to noise but only applies to their wedge phantom.

TABLE IX. A direct comparison of the average calcification CNR of the three calcification sizes (230–280, 280–330, and 330–380  $\mu\text{m}$ ) over three glandular ratios of 30%, 45%, and 70% in the LE image and DE calcification images without/with scatter correction (pinhole-array interpolation method and algorithmic method). The CNR values of DE calcification images with algorithmic scatter correction and denoised techniques are also listed.

Glandular (%)	Calcification ( $\mu\text{m}$ )	CNR			
		DE/o	DE-pin	DE-al	DE-al-de
30	230–280	0.31	0.70	0.67	1.02
	280–330	0.49	0.80	1.00	1.54
	330–380	0.44	1.35	1.47	2.12
45	230–280	0.36	0.93	1.09	1.28
	280–330	0.66	1.44	1.61	2.23
	330–380	0.51	1.56	1.68	2.10
70	230–280	0.26	0.76	0.84	1.30
	280–330	0.43	1.35	1.46	2.07
	330–380	0.56	1.87	2.09	2.74

The interpolation method may be more practical for different phantoms. Scattered radiation was estimated independently for each pinhole, and therefore more noise was recorded in the scatter signals. In this paper, we used cubic spline interpolation, which we found to be optimal, over linear and nearest-neighbor interpolation.

The algorithmic scatter correction method proposed here is based on the fact that the scatter component in mammograms is a quantity of low-frequency and most pixels in mammograms are noncalcification pixels. This method is verified by calcification and breast phantoms with fixed thickness. Since breast is usually compressed to a uniform thickness  $T$  in a mammographic examination, the assumption of low-frequency is valid in most area away from the skin margins in a mammogram. The method only uses the information of LE and HE images, and it is a pure algorithmic method where there is no extra exposure. If this method could be used in practice, there is no external or internal hardware modification to be made on the mammography system. However, if we use the pinhole-array interpolation method for scatter correction, two more exposures with lead sheet should be necessary, which complicates the system.

With the algorithmic scatter correction method, the sampled pixels are considered as noncalcification pixels whose corresponding  $t_c$  are zero. In our experiment, the sampling interval was around 60–120 pixels, 60 pixels being used close to edge and 120 pixels being used in the central part, which resulted in good performance. We have conducted the algorithmic scatter correction with much denser and sparser distribution of sample pixels. When a uniform sampling with 50 pixels interval was used, a singular matrix was generated. For the case of nonuniform sampling interval 50–70 pixels we observed no reduction of the ROI signals and ROI rms, indicating that too many sampling pixels were unwanted. On the other hand, if the sampling interval was over 200 pixels, the sampled pixels were not sufficient to produce reasonable scatter intensity field. Thus, the effectiveness of the algorithmic method is influenced by which pixels are sampled. If too many pixels are sampled, there is an increased chance that some of the pixels will be from calcifications and not the background. Further, oversampling the pixels will generate similar equations in the equation set and this may lead to a singular matrix. On the other hand, if the number of sampled pixels is too small, the reasonable scatter intensity fields cannot be estimated. At best, the sampling interval should be no less than 60 pixels and no greater than 120 pixels; denser and sparser samplings were used close to edge and in the central part of the phantom, respectively.

Although our algorithmic scatter correction method is effective, there are some fluctuations of background signal in scatter-corrected DE calcification images. These errors came from scatter correction, quantum noise, and fitting errors. The scatter estimate introduced additional noise variance into the corrected image beyond that from the uncorrected image. However, quantum noise is the major source of variation of background DE calcification signals since approximately half the dose of the conventional mammography screening was applied to the LE or HE image acquisition and the noise in LE

and HE images both contribute to the DE calcification image. Prefiltration of LE and HE images or post image processing of DE calcification images may further reduce the noise fluctuations in DE calcification images,<sup>15,17</sup> we implemented the denoising techniques in our present study. In the case of applying median filter (kernel = 5) to the HE image, fluctuations of background signal in scatter-corrected DE calcification were reduced (Table VIII). Additionally, the fitting errors exist in the background signal deviations. According to the fitting residuals listed in Sec. 3.C and considering the DE calculation using Eq. (4) is not an accurate interpolation procedure, we assumed the fitting error to be 50  $\mu\text{m}$ .

## 5.B. Calcification CNRs

After using the proposed algorithmic scatter correction method and denoising technique, the calcification CNR can be improved greatly. The clearly visible calcification size can be reduced from 380 to 280  $\mu\text{m}$ . Calcifications smaller than 280  $\mu\text{m}$  were not visible in most cases. Numerical calculations with idealized detector systems have estimated the calcification size detection threshold with DE imaging to be around 200–250  $\mu\text{m}$ .<sup>9,12</sup> Our experimental estimates for the detectable calcification size of 280  $\mu\text{m}$  with DEDM are in reasonable agreement with these numerical studies.

We can find the threshold of calcification size that can be visualized with DE imaging, utilizing the mammography system and dose level tested, there does not appear to be an improvement of the conventional single energy mammography. Previous investigations<sup>22,23,37</sup> have shown that the lower CNR in DE calcification image is mainly caused by the quantum noise. In DEDM, approximately half the dose of the conventional mammography screening was applied to the LE or HE image acquisition and the noise in LE and HE images both contribute to the DE calcification image. Therefore, DE image has higher intrinsic quantum noise theoretically.<sup>9</sup> Quantum noise reduction is an independent work, not within the scope of this work. On the other hand, the threshold of calcification size with conventional single energy mammography may vary across the image and increase for regions with complex tissue structures. The main advantage of DE imaging lies in its ability to suppress the contrast between different tissue structures and depict calcifications in a largely uniform background, so the threshold size with DEDM remains more uniform across the image.

## 5.C. Limitations of the study

From the experimental results, it can be seen that this algorithmic method has similar or even better performance than the pinhole-array interpolation method and it is effective in scatter correction for DEDM. However, the proposed algorithmic method has not been fully validated because of the limited experimental conditions. The first limitation concerns the lack of images with structured background, so the effect of the proposed method in a scenario where DEDM is clinically applicable is unknown. In the present study, a homogeneous phantom was used for both imaging and calibration for

avoiding calibration phantom errors which have a serious effect on calcification imaging in DEDM.<sup>21,22</sup> The proposed scatter correction method works well where there is no calibration phantom error. If we use a semianthropomorphic phantom (structured background) for imaging, the calibration should be done using a separate homogeneous phantom which may result in calibration phantom errors which may be large. In this study, we would like to investigate scatter correction independently, so we used the same phantom for both calibration and imaging. Nevertheless, reduction of calibration phantom errors is a part of our ongoing work. If we get some results of reduction of calibration phantom errors, we will evaluate the proposed scatter correction method where DEDM is really used.

The second concern has to do with the different thicknesses and sizes of phantoms where the proposed method should be evaluated. The compressed breasts have different thicknesses and sizes under clinical conditions. In this study, we used  $12 \times 10 \times 5 \text{ cm}^3$  and  $12 \times 10 \times 4 \text{ cm}^3$  phantoms to validate our proposed algorithm. However, 5 cm is the average thickness when the breast is compressed and most commercially available physical breast phantoms are of the similar size ( $12 \times 10 \text{ cm}^2$ ). Therefore, the phantom used in this study was representative. Since SPR increases with breast thickness and it is particularly relevant for breast thicknesses over 5 cm, further investigations are needed to validate the proposed method in different phantom thicknesses and sizes.

In the present study, there is no guarantee of the same effect if the proposed algorithmic method was applied in cases where DEDM is really applicable, because of the limited experimental conditions. In the future study, the proposed scatter correction method should be combined with the reduction of calibration phantom error and evaluated fully under clinical conditions.

## 6. CONCLUSION

An algorithmic scatter correction method for DEDM has been developed and implemented using a commercially available full-field digital mammography system. This method is based on the fact that the scatter component in mammograms is a quantity of low frequency and that most pixels in mammograms are noncalcification pixels. The method only uses the information from the LE and HE images and it does not require extra exposures with a lead sheet. It is convenient and there is no extra dose to patients. The results show that the algorithmic scatter correction method is effective and has similar performance to pinhole-array interpolation method. When applying the scatter correction to images, the resultant background DE calcification signals can be reduced. Under the current implementation of DEDM, utilizing the mammography system and dose level tested, the clearly visible calcification size can be reduced from 380 to 280  $\mu\text{m}$ . Calcifications smaller than 280  $\mu\text{m}$  were not visible in most cases. The calcification smaller than 230  $\mu\text{m}$  were not visible. The visibility of calcifications in DE calcification images was limited by the quantum noise in the LE and HE images.

Although the proposed scatter correction method is effective, it is just validated by a 5-cm-thick phantom with calcifications and homogeneous background. In the present study, because of the limitations of the experimental conditions, many clinical conditions such as structured background, different thicknesses, and sizes were not considered. The proposed scatter correction method should be combined with the reduction of calibration phantom error and evaluated under clinical conditions in the future work.

## ACKNOWLEDGMENTS

The authors thank Hao Yan, Ph.D., for his Monte Carlo simulation with this work. This work was supported in part by the National Natural Science Foundation of China (Grant No. 61172163) and the Doctoral Fund of the Education Ministry of China (Grant No. 20110201110011). Robert M. Nishikawa is a shareholder in, a consultant to, and receives royalties from Hologic, Inc. He is also a consultant to iCAD.

- a) Present address: Department of Radiology, University of Pittsburgh, Pittsburgh, Pennsylvania, 15213
- b) Present address: Department of Radiology, Stony Brook University, Stony Brook, New York 11794
- c) Electronic mail: xqmou@mail.xjtu.edu.cn
- <sup>1</sup> A. Fandos-Morera, M. Prats-Esteve, J. Tura-Soteras, and A. Traveria-Cros, "Breast tumors: Composition of microcalcifications," *Radiology* **169**, 325–327 (1988).
- <sup>2</sup> P. C. Johns, D. J. Drost, M. J. Yaffe, and A. Fenster, "Dual-energy mammography: Initial experimental results," *Med. Phys.* **12**, 297–304 (1985).
- <sup>3</sup> S. C. Kappadath and C. C. Shaw, "Quantitative evaluation of dual-energy digital mammography for calcification imaging," *Phys. Med. Biol.* **49**, 2563–2576 (2004).
- <sup>4</sup> R. E. Alvarez and A. Macovski, "Energy-selective reconstructions in X-ray computerized tomography," *Phys. Med. Biol.* **21**, 733–744 (1976).
- <sup>5</sup> L. A. Lehmann, R. E. Alvarez, A. Macovski, and W. R. Brody, "Generalized image combinations in dual KVP digital radiography," *Med. Phys.* **8**, 659–667 (1981).
- <sup>6</sup> W. R. Brody, G. Butt, A. Hall, and A. Macovski, "A method for selective tissue and bone visualization using dual energy scanned projection radiography," *Med. Phys.* **8**, 353–357 (1981).
- <sup>7</sup> P. C. Johns and M. J. Yaffe, "Theoretical optimization of dual-energy x-ray imaging with application to mammography," *Med. Phys.* **12**, 289–296 (1985).
- <sup>8</sup> E. L. Gingold and B. H. Hasegawa, "Systematic bias in basis material decomposition applied to quantitative dual-energy x-ray imaging," *Med. Phys.* **19**, 25–33 (1992).
- <sup>9</sup> M. R. Lemacks, S. C. Kappadath, C. C. Shaw, X. Liu, and G. Whitman, "A dual-energy subtraction technique for microcalcification imaging in digital mammography—A signal-to-noise analysis," *Med. Phys.* **29**, 1739–1751 (2002).
- <sup>10</sup> H. N. Cardinal and A. Fenster, "An accurate method for direct dual-energy calibration and decomposition," *Med. Phys.* **17**, 327–341 (1990).
- <sup>11</sup> D. P. Chakraborty and G. T. Barnes, "An energy sensitive cassette for dual-energy mammography," *Med. Phys.* **16**, 7–13 (1989).
- <sup>12</sup> J. M. Boone, G. S. Shaber, and M. Tecotzky, "Dual-energy mammography: A detector analysis," *Med. Phys.* **17**, 665–675 (1990).
- <sup>13</sup> D. S. Brettle and A. R. Cowen, "Dual-energy digital mammography using stimulated phosphor computed radiography," *Phys. Med. Biol.* **39**, 1989–2004 (1994).
- <sup>14</sup> S. C. Kappadath and C. C. Shaw, "Dual-energy digital mammography: Calibration and inverse-mapping techniques to estimate calcification thickness and glandular-tissue ratio," *Med. Phys.* **30**, 1110–1117 (2003).
- <sup>15</sup> S. C. Kappadath and C. C. Shaw, "Dual-energy digital mammography for calcification imaging: Scatter and nonuniformity corrections," *Med. Phys.* **32**, 3395–3408 (2005).

- <sup>16</sup>S. C. Kappadath, C. C. Shaw, C.-J. Lai, X. Liu, G. Whitman, and W. T. Yang, "Dual-energy digital mammography for calcification imaging: Improvement by post-image processing," *Proc. SPIE* **5745**, 1342–1350 (2005).
- <sup>17</sup>S. C. Kappadath and C. C. Shaw, "Dual-energy digital mammography for calcification imaging: Noise reduction techniques," *Phys. Med. Biol.* **53**, 5421–5443 (2008).
- <sup>18</sup>A. Taibi, S. Fabbri, P. Baldelli, C. di Maggio, G. Gennaro, M. Marziani, A. Tuffanelli, and M. Gambaccini, "Dual-energy imaging in full-field digital mammography: A phantom study," *Phys. Med. Biol.* **48**, 1945–1956 (2003).
- <sup>19</sup>K. Bliznakova, Z. Kolitsi and N. Pallikarakis, "Dual-energy mammography: Simulation studies," *Phys. Med. Biol.* **51**, 4497–4515 (2006).
- <sup>20</sup>M.-E. Brandan and V. Ramírez-R, "Evaluation of dual-energy subtraction of digital mammography images under conditions found in a commercial unit," *Phys. Med. Biol.* **51**, 2307–2320 (2006).
- <sup>21</sup>X. Mou and X. Chen, "Error analysis of calibration materials on dual energy mammography," *Medical Image Computing and Computer-Assisted Intervention MICCAI 2007*, Lecture Notes in Computer Science, Vol. 4792, 2007, pp. 596–603.
- <sup>22</sup>X. Mou, X. Chen, L. Sun, H. Yu, Z. Ji, and L. Zhang, "The impact of calibration phantom errors on dual-energy digital mammography," *Phys. Med. Biol.* **53**, 6321–6336 (2008).
- <sup>23</sup>V. N. Cooper III, J. M. Boone, J. A. Seibert, and C. J. Pellot-Barakat, "An edge spread technique for measurement of the scatter-to-primary ratio in mammography," *Med. Phys.* **27**, 845–853 (2000).
- <sup>24</sup>K. Nykänen and S. Siltanen, "X-ray scattering in full-field digital mammography," *Med. Phys.* **30**, 1864–1873 (2003).
- <sup>25</sup>A. Krol, D. A. Bassano, C. C. Chamberlain, and S. C. Prasad, "Scatter reduction in mammography with air gap," *Med. Phys.* **23**, 1263–1270 (1996).
- <sup>26</sup>Z. Jing, W. Huda, and J. K. Walker, "Scattered radiation in scanning slot mammography," *Med. Phys.* **25**, 1111–1117 (1998).
- <sup>27</sup>X. Liu, C. C. Shaw, C.-J. Lai, M. C. Altunbas, L. Chen, T. Han, and T. Wang, "Scatter rejection and low-contrast performance of a slot-scan digital chest radiography system with electronic aft-collimation: A chest phantom study," *Med. Phys.* **35**, 2391–2402 (2008).
- <sup>28</sup>G. T. Barnes, X. Wu, and A. J. Wagner, "Scanning slit mammography," *Med. Prog. Technol.* **19**, 7–12 (1993).
- <sup>29</sup>X. Chen, X. Mou, H. Yan, H. Yu, and L. Zhang, "Scatter correction algorithm without extra exposure for dual-energy digital mammography," *Proc. SPIE* **7258**, 725840 (2009).
- <sup>30</sup>X. Chen, R. M. Nishikawa, S. Chan, B. A. Lau, L. Zhang, and X. Mou, "Algorithmic scatter correction in dual-energy digital mammography for calcification imaging," *Proc. SPIE* **8313**, 83130E (2012).
- <sup>31</sup>G. R. Hammerstein, D. W. Miller, D. R. White, M. E. Masterson, H. Q. Woodard, and J. S. Laughlin, "Absorbed radiation dose in mammography," *Radiology* **130**, 485–491 (1979).
- <sup>32</sup>F. Salvat, J. M. Fernández-Varea, and J. Sempau, PENELOPE, a code system for Monte Carlo simulation of electron and photon transport, OECD Nuclear Energy Agency, Issy-les-Moulineaux, France, 2006.
- <sup>33</sup>J. Sempau, E. Acosta, J. Baró, J. M. Fernández-Varea, and F. Salvat, "An algorithm for Monte Carlo simulation of coupled electron-photon transport," *Nucl. Instrum. Methods Phys. Res. B* **132**, 377–390 (1997).
- <sup>34</sup>I. Kawrakow and D. W. O. Rogers, "The EGSnrc code system: Monte Carlo simulation of electron and photon transport," NRCC Report PIRS-701, 2007 (available URL: <http://www.irs.inms.nrc.ca/EGSnrc/pirs701/index.html>).
- <sup>35</sup>A. P. Colijn and F. J. Beekman, "Accelerated simulation of cone beam X-Ray scatter projections," *IEEE Trans. Med. Imaging* **23**, 584–590 (2004).
- <sup>36</sup>T. Luo, X. Mou, and S. Tang, "An applicability research on JND model," *Proc. SPIE* **6146**, 614610 (2006).
- <sup>37</sup>X. Chen, R. M. Nishikawa, S. Chan, L. Zhang, and X. Mou, "Image noise sensitivity of dual-energy digital mammography for calcification imaging," *Proc. SPIE* **7961**, 796155 (2011).